

## **Hydrothermal signature in ferromanganese oxide coatings on pumice from the Central Indian Ocean Basin**

Niyati G. Kalangutkar\*, Sridhar D. Iyer, Maria B.L. Mascarenhas-Pereira, B. Nagender Nath

Corresponding author: N.G. Kalangutkar, (e-mail: [niyati.kalangutkar@gmail.com](mailto:niyati.kalangutkar@gmail.com)),

Tel.: +91-832-2525543, Fax: +91-832-2525566),

Council of Scientific and Industrial Research, National Institute of Oceanography, Dona Paula, Goa 403004, India . *Present address*: N.G. Kalangutkar, National Centre for Antarctic and Ocean Research (MoES), Headland Sada, Vasco-da-Gama, Goa 403804, India

### **Abstract**

Mineralogical and elemental analyses of 20 ferromanganese (FeMn) coated pumice samples from the Central Indian Ocean Basin (CIOB) indicate that todorokite is the major mineral phase, whereas vernadite occurs only rarely. Based on major, trace and rare earth elements (REEs) as well as Ce anomalies, the sources of the FeMn oxides were identified to be either hydrogenous, hydrothermal-plume fallout, diagenetic or a combination of these. Plots of Fe/Mn vs. Ce or Co reveal a distinct demarcation of the diagenetic, hydrogenous and plume fallout samples. Five samples are interpreted to be of hydrothermal origin because these show negative Ce anomalies and low Co/Zn ratio (0.5 to 1.1), and are masked by diagenesis. The relative contributions of hydrogenous, hydrothermal and diagenetic inputs were assessed in terms of ternary mixing patterns using REE mass balance equations. Furthermore, the hypothetical Ce anomaly ( $Ce/Ce^*$ ) was calculated using ternary mixing calculations for hydrogenous: hydrothermal:diagenetic end-members to ascertain the input to FeMn oxides on the pumice samples. This revealed a distinction between hydrogenous and hydrothermal components but diagenetic and plume fallout components could not be distinguished because this scheme comprises a three end-member calculation. A conservative estimate indicates the hydrothermal component to vary between 24% and 72%. The growth rates of the oxides, as estimated from published empirical methods, range between 3 and 47 mm/10<sup>6</sup> years. Fe/Mn ratios yielded a maximum age of 5-7 Ma and a minimum of 0.04-0.1 Ma. This suggests that the commencement of accretion of the FeMn oxides generally precedes the age of the Krakatau 1883 eruption, which is commonly considered as being the prime source of pumice to CIOB. This is the first evidence of hydrothermal influence in the formation of FeMn oxides on CIOB pumice.

*Electronic supplementary material* The online version of this article ([doi:10.1007/s00367-015-...](https://doi.org/10.1007/s00367-015-...)) contains supplementary material, which is available to authorized users.

## **1. Introduction**

Ferromanganese (FeMn) nodules and crusts of the Central Indian Ocean Basin (CIOB) have been explored by several researchers in terms of their abundance, morphology, mineralogy, chemistry, grade, etc. (e.g., Cronan and Moorby 1981; Nath et al. 1992, 1994; Mukhopadhyay et al. 2008 ; Sharma et al. 2010; Pattan et al. 2013). The role of microorganisms in the genesis of manganese nodules was reported by Wang et al. (2009) for nodules of Clarion-Clipperton Zone and similar observation were made by Nayak et al. (2013) for CIOB nodules. The nodules have nuclei comprised of basalt, clay, pumice and shark teeth (Sarkar et al. 2008). Moreover, ferromanganese nodules and crusts collected using free-fall grabs, Pettersson grabs and dredges at several CIOB sites are commonly characterized by pumice. It has been reported that nodules with pumice nuclei has the thinnest FeMn oxide layer and a higher oxide grade compared to the nodules with other types of nuclei (Nath 2007; Vineesh et al. 2009). Despite this wealth of knowledge, to date there are no published records of hydrothermal events in the CIOB based on the analyses of nodules. The present detailed study is the first to attempt unravelling the origin of FeMn oxides coating CIOB pumice.

The existence of a large field (600,000 km<sup>2</sup>) of pumice in the CIOB and the occurrence of pumice as nuclei within the FeMn nodules have been reported by Iyer and Karisiddaiah (1988), Iyer and Sudhakar (1993) and Sarkar et al. (2008). The pumices examined were recovered from an average water depth of 5,000 m at 72–80°E, 9–16°S during numerous cruises spanning the time period 1981–1996. In several cases, the samples were taken close to seamounts or fracture zones, and have up to 5-mm-thick FeMn oxides.

Recently, Pattan et al (2013) reported the origin of the FeMn coated pumice based on the composition and comparison with known Toba eruptions. Within this context, the purpose of this paper is to explore the sources and processes that operated during the accretion of the oxides on CIOB pumice. This is based on mineralogical and elemental analyses, assessments of the nature and growth rate of the FeMn oxides, and estimates of their age when accretion of oxides commenced on the pumice. Here we evaluate the approximate age and source of the overlying FeMn oxides.

## **2. Study area**

The CIOB can be subdivided into two distinct regions: a highly deformed area north of 9°S and relatively undeformed north-eastern and southern parts south of 9°S. The study area (Fig. 1) is traversed

by a number of fault zones and seamounts located along N–S trending propagative fractures. The density of seamounts is higher near the 79°E fault zone, where the seamounts have an average height of 500 m and are multi-peaked, with an elongated base as well as moderate to high basal areas, slope angles and volumes. By contrast, their counterparts further away from this fault zone are generally taller, larger and more conical. The flank cones at the base of the multi-peaked seamounts could reflect their formation from later eruptions (Das et al. 2007).

In the study area, nodules with pumice nuclei occur mainly along either side of the fault zones at 76°30'E and 79°E, and at 10°30'–14°30'S (Fig. 1; Vineesh et al. 2009). They are also abundant between the seamount chains (Iyer and Sudhakar 1993).

### **3. Materials and methods**

#### **3.1 Analytical methods**

In all, 676 pumice samples were examined of which about 25% were coated with FeMn oxides. Of these, 20 representative samples with substantial FeMn oxide coatings were selected for detailed investigations (Fig. 1, Table 1). The samples were washed, dried and their surface features observed under a binocular microscope. The FeMn oxides were scraped and made sea-salt free by keeping the samples immersed in distilled water for a couple of days. The presence/absence of sea salt was tested by  $\text{AgNO}_3$ . Later the samples were cleaned in an ultrasonic bath for 10 minutes to disperse any possible sediments adhered. The oven dried oxide was finely ground using an agate mortar and pestle. The powders were used for X-ray diffraction (XRD) and chemical analyses. The samples were heated to ~60 °C to allow the adhered moisture to escape and XRD was carried out using a Rigaku XRD (Ultima IV) apparatus with  $\text{CuK}\alpha$  as target and scanning between 8° and 80° 2 $\theta$  at a speed of 3° 2 $\theta$  per minute. To help resolve the X-ray lines the experiment was repeated by heating the samples to 105 °C for 48 h and then subjected to XRD analysis following the method of Burns et al. (1983), Usui et al. (1997) and Glasby et al. (1997).

The samples were mounted on stubs, and examined under a scanning electron microscope (SEM) and analyzed with an energy dispersive spectrometer (EDS). The SEM system was a JEOL JSM 5800 LV fitted with an INCA EDS, operating at 20 kV with a working distance of 20 mm for SEM and 10 mm for EDS observations.

The sample powders were digested following the methodology of Balaram and Rao (2003), and 5 ml of 1 ppm rhodium tracer served as internal standard. Each aliquot was topped up to 100 ml using distilled water and was analyzed for trace elements and rare earth elements (REEs) by means of an inductively coupled plasma-mass spectrometer (Perkin Elmer's Elan DRC-II ICP-MS) at the National Geophysical Research Institute, Hyderabad. Precision based on duplicate samples was found to be better than  $\pm 3\%$ .

Fe and Mn were determined on an inductively coupled plasma-optical emission spectrometer (Perkin-Elmer Optima-2000 DV ICP-OES) at the National Institute of Oceanography, Goa. Precision was  $\pm 6\%$  for Mn and  $\pm 2\%$  for Fe. Also the measured values of the reference standard USGS NOD A-1 values are on par with the reported values. A blank solution served to correct for any contamination during sample preparation, and run after every five samples.

#### **4. Results**

The 676 pumice samples vary in length from 1 to 14 cm and about 25% of these have FeMn oxides occurring as a thin film or botryoidal coating up to 5 mm thick (Fig. 2; Kalangutkar 2012). By comparison, Sudhakar et al. (1992) reported that 16% of their 3,083 pumice samples were either coated with FeMn oxides or occurred as nuclei in nodules.

Binocular microscopy and SEM images reveal well-formed botryoids of FeMn oxides (Fig. 3a–c). The patchy oxide coats and botryoidal structure suggest accretion by colloidal formation. Radiolarians and phillipsite (Fig. 3d) were included at later stage within the vesicles. Phillipsite is a mineral formed essentially during diagenesis. The XRD analyses of these oxides show todorokite as a major phase; vernadite was observed in a few samples (see ESM Fig. 1 available online as electronic supplementary material for this article) before the heating experiment was carried out. After heating, results show a shift in the todorokite peak. The intensity of todorokite peaks decreased and minor peaks of birnessite could be identified in a few samples along with crystalline sharper peaks of goethite, magnetite, lepidocrocite and hematite in some samples (Fig. 4). Plagioclase (oligoclase-labradorite) and quartz also occur as minor minerals (cf. Kalangutkar et al. 2011; Kalangutkar 2012). The chemical compositions of the FeMn oxides are reported in Table 2 and ESM Table 1 of the online electronic supplementary material, and selectively plotted for interpretation (cf. below). Manganese contents range from 3.4 to 29.7 wt% and iron contents from 2.1 to 11.6 wt%. The Mn/Fe ratio varies between 1.04 and 9.37. A comparison of the present trace element values with those of Cronan (1980) and Cronan and Moorby (1981) (Co=1,130, Cu=9,910, Cr=36, Zn=1,190 and Pb=650 ppm) show close similarity. Most of the

samples show both hydrogenetic and diagenetic origin for the FeMn oxides on the ternary diagram of  $(\text{Co}+\text{Ni}+\text{Cu})\times 10-\text{Fe}-\text{Mn}$  in Fig. 5 (cf. Halbach et al. 1981). The REE data (Table 3), after normalising with PAAS (post-Archean Australian shale), largely exhibit a positive Ce anomaly (Fig. 6) except for five samples (samples #4, 6, 17, 18, 20) that have negative Ce anomaly and low Co/Zn ratio. The ratios of Mn/Fe vs. Co (Fig. 7a) and Mn/Fe vs. Ce (Fig. 7b) were plotted to discriminate diagenetic and hydrogenetic end-members. In Fig. 7 some samples (#4, 11, 12, 13, 14, 16) do not follow the hydrogenetic-diagenetic trend.

Growth rates (R) were estimated by using the empirical formulae of Lyle (1982), Sharma and Somayajulu (1987) and Manheim and Lane-Bostwick (1988), which are  $R=16[(\text{Mn})/(\text{Fe})^2]+0.448$ ,  $R=8.33[\text{Mn}/(\text{Fe})^2]+2.16$  and  $R=0.68/\text{Co}(50/\text{Fe}+\text{Mn})^{1.67}$  respectively. Correspondingly the FeMn oxides show growth rates ranging from 3 to 47 (avg. 10), 3 to 27 (avg. 7), and 3 to 19 mm/10<sup>6</sup> years (avg. 5 mm/10<sup>6</sup> years), implying ages of 0.07 to 5.64 Ma, 0.04 to 6.44 Ma, 0.08 to 7.9 Ma respectively (Table 2).

## 5. Discussion

### 5.1 Mineralogy and elemental composition

Vernadite (Koschinsky and Hein 2003) as well as todorokite (Usui et al. 1997) occur near hydrothermal vent sites. Also the abundance of todorokite can increase during diagenesis because of partial conversion of vernadite to todorokite (Bodeř et al. 2007). Moreover, vernadite will also form when the FeMn oxides precipitate from far field hydrothermal plumes. Therefore, according to Canet et al. (2008) oxide mineralogy is not a major discriminating factor to identify a hydrothermal influence to understand the genesis of the FeMn oxides. The patchy oxide coats and botryoidal structure of FeMn suggest accretion by colloidal formation. The pumice samples usually contain clay, within the vesicles, which has ion exchange properties that facilitate adsorption of transition metals and REEs onto the surface of the pumices for the accretion of the FeMn oxides and this process is aided by the colloids of oxyhydroxides (cf. Nath 2007). Fe-oxyhydroxides have a tendency to grow epitaxially with vernadite (Nath et al. 1994; Kuhn et al. 1998). In FeMn oxide these iron-bearing phase is usually described as cryptocrystalline or amorphous hydrated Fe-oxide or ferrihydrite (Crerar and Barnes 1974; Glasby 1972). The possible hump in the XRD patterns of all the samples at about 20° 2θ could reveal the existence of amorphous materials with poor crystallinity. On heating, the ferrihydrite converts to goethite, and magnetite phases

which on progressive heating converts to hematite due to dehydration. Before the heating experiment todorokite was observed to be the major phase.

Todorokite has peaks at around 10 Å and 5Å and may be directly precipitated from low-temperature hydrothermal solutions (Kuhn et al. 2003). However, todorokite can also form under diagenetic growth (Burns and Burns 1979; Bodeř et al. 2007). But 10Å + 5Å peaks are also typical for busserite and 7Å + 3.5Å reflections for birnessite. Both these minerals typically form during diagenetic growth. But, samples #14 and 16 do not show reflections at 10 Å or 7Å which are typical of diagenetic process, but both seem to have reflections around 2.4 Å which could have formed under hydrothermal process. On heating the samples, the intensity of todorokite peaks decreased and minor peaks of birnessite could be identified in a few samples. Whereas, plume fallout samples (1, 4, 11, 13, 14 and 16) showed sharper peaks of crystalline minerals of goethite, magnetite, lepidocrocite and hematite. The other samples show the presence of todorokite, vernadite and/or birnessite. The presence of birnessite in a few samples shows that masking of hydrothermal signatures by diagenesis.

Since the Mn/Fe ratio can be used as an indicator of source for the oxides (Calvert and Price 1977), this ratio in the studied oxides (1.04 to 9.37) also attests to a possible hydrogenetic and hydrogenetic-diagenetic source (Fig. 5). The PAAS normalized REE data reveal a negative Ce anomaly for five samples (#4, 6, 17, 18, 20; Fig. 6), whereas remaining samples show a positive Ce anomaly.

The negative Ce anomaly is possibly due to enhanced accretion of oxides. Such a situation is possible either if the oxides have formed (1) by diagenesis when the pumices were buried in the seafloor sediments or (2) under hydrothermal conditions or (3) have a diagenetic-hydrothermal influence that could account for the samples with a high growth rate of oxides. Considering the diagenetic influence on the samples, it is possible that the negative Ce anomaly could be a result of diagenesis in an oxic environment. But, however these samples with negative Ce anomaly also have a low Co/Zn (0.52 to 1.1, Table 2) ratio. Co/Zn value less than or close to 1 is indicative of hydrothermal source (cf. Toth 1980). Which suggest that the low Ce anomaly is not due to diagenesis alone but may be a result of hydrothermal input. The Co/Zn ratio (0.52 to 1.1) of the above five samples are similar to those reported for the Rodriguez Triple Junction (RTJ; 0.83 to 1.55; Nath et al. 1997) and the Central Indian Ridge (CIR; 1.2 to 1.79; Kuhn et al. 1998) hydrothermal ferromanganese crusts. However, the present CIOB samples show a higher Co+Ni+Cu and Fe/Mn (3,457 to 19,091 ppm and 1.04 to 9.37 respectively). The higher (Ni + Cu) content especially of the samples with significant hydrothermal contribution is

evidence for an increased diagenetic input and is also supported by the positive correlation of Ni and Cu with Mn/Fe. The RTJ (Co+Ni+Cu, 1200 to 1300 ppm; Fe/Mn, 0.34 to 0.51; Nath et al. 1997) and CIR FeMn (Co+Ni+Cu, 2173 to 3409 ppm; Fe/Mn, 0.64 to 0.78; Kuhn et al. 1998) crusts, formed on hard rock substrate and without any diagenetic input that exhibited negative Ce anomaly but paradoxically the concentrations of major and minor elements were distinctive of hydrogenetically formed FeMn oxides. Nath et al. (1997) and Kuhn et al. (1998) attributed these crust samples to be of mixed hydrothermal-hydrogenetic nature. On similar lines, five of our samples (samples #4, 6, 17, 18, 20) also have a mixed hydrothermal-diagenetic nature. Due to higher hydrothermal component henceforth these five samples will be termed as 'hydrothermal samples' in the manuscript.

The samples are affected by diagenesis and also probably by hydrogenetic processes (Fig. 5). The ratios of Mn/Fe vs. Co (Fig. 7a) and Mn/Fe vs. Ce (Fig. 7b) were plotted to distinguish diagenetic and hydrogenetic end-members. The inverse correlation with a parabolic patterns of Ce and Co are characteristic for elements enriched by oxidative scavenging and the process is mainly dependent on the growth rate, i.e., lower the growth rate more the time available for the slow process of scavenging. Therefore, with respect to Co and Ce there is a continuum between the hydrogenetic end-member with slow growth rates and the diagenetic end-member with high growth rates (Halbach et al. 1983; Manheim and Lane-Bostwick 1988; Takahashi et al. 2007).

It is observed that four (sample #6, 17, 18, 20) of the five samples which have negative Ce anomaly and low Co/Zn fall along the diagenetic end of the continuum (Fig. 7), indicating an imprint of hydrothermal signatures followed by diagenetic process. But, some samples (#4, 11, 12, 13, 14, 16) do not follow the hydrogenetic-diagenetic trend and have trace elements, REEs and Co/Zn ratios between those of the hydrothermal (#4, 6, 17, 18, 20) and hydrogenous (#5, 9, 10, 19) samples and have a lower (Co+Ni+Cu, 0.35 to 0.94 wt%). These samples have diluted trace and REE signatures that could represent a hydrothermal-plume fallout contribution with less diagenetic influence. A similar plume fallout influence was observed in FeMn micronodules along the East Pacific Rise and Mid-Atlantic Ridge (Dekov et al. 2003). Those authors suggested that when the hydrothermal suspended matters comes in contact with large volumes of seawater, extensive scavenging occurs which masks the hydrothermal signal with increasing distance from the source and apparently enhances the hydrogenous character. Samples (#14 and 16) with lowest Co and Ce contents have vernadite, goethite and lepidocrocite as confirmed from XRD analysis. Given that the samples show hydrogenous, hydrothermal and diagenetic

influence, we assessed the relative contribution of each of these processes by using ternary mixing equations and mass balance equations (Chavagnac et al. 2005; Mascarenhas-Pereira and Nath 2010; modified from Albarède 1995).

## 5.2 Evidence for hydrothermal signatures

### 5.2.1 Mixing calculation using REEs

The studied FeMn oxides show a positive middle REE (MREE) trend that indicates their incorporation during diagenesis and hydrogenous precipitation (cf. Nath et al. 1992, 1994). In view of the fact that no hydrothermal nodule or crust from the CIOB is reported and available for use as the end-member, the hydrothermal Mn-oxide data (Nath et al. 1992) from the Lau Basin is used as one of the end-members for mixing calculation for this study. A similar ternary mixing equation using three end-member (terrigenous:sulphide:MORB) has been successfully carried out for a CIOB sediment core using data from East Pacific for the sulphide end-member. The use of different sulphide end-members had little variation in the calculated percentages (Mascarenhas-Pereira and Nath 2010).

The REE mixing calculation for hydrogenous, hydrothermal and diagenetic end-members for the present study is given as

$$f_{\text{Hydrogenous}} + f_{\text{Hydrothermal}} + f_{\text{Diagenetic}} = 1 \quad (1)$$

and

$$C_{\text{mix}}^i = (f_{\text{Hydrogenous}} \times C_{\text{Hydrogenous}}^i) + (f_{\text{Hydrothermal}} \times C_{\text{Hydrothermal}}^i) + (f_{\text{Diagenetic}} \times C_{\text{Diagenetic}}^i)$$

where  $f$  represents the proportion of each end-member contributing to the oxides and  $C_{\text{mix}}^i$  is the concentration of element  $i$  in the mixture.

The three end-members used are (cf. Nath et al. 1992) (1) the average of nine hydrogenetic FeMn crusts from the CIOB (Nath 1993), (2) hydrothermal Mn-oxide from the Lau Basin (Mn% = 49.63; total REE = 12.04 ppm, with major birnessite phase and minor todorokite and  $\delta\text{MnO}_2$  (Nath 1993) and (3) a diagenetic nodule (Nath et al. 1992) with a typically todorokite mineralogy and a high Mn/Fe ratio (>3.3). The results display the shale normalised REE patterns with positive Ce anomaly while the negative Ce anomaly could not be reproduced (Fig. 8). This is due to the higher REE content (by 2 orders of magnitude) in the hydrogenous end-member over that of hydrothermal end-member. Thus, the REE mixing calculations could be performed only for those samples which had a positive Ce anomaly.



The shale normalised REE patterns for the studied samples are reproducible using a mixture of 10:72:18 to 80:16:4 of hydrogenous:hydrothermal:diagenetic content respectively. Variations in the proportions of hydrogenous:hydrothermal:diagenetic components can be explained by the samples having been recovered from a large geographical area.

### 5.2.2 Mixing calculation using Ce anomaly

Mixing calculations using Ce anomaly have not been previously attempted and these may provide clues for hydrothermal derivation of FeMn oxides. Since the calculations with whole REE data could not resolve the relative proportion of each end-member samples with negative Ce anomalies, the relative proportions of the three end-members were calculated (see ESM Table 2 in the online electronic supplementary material) by using the Ce anomaly. Though it is known that Ce typically responds to oxygenation changes in the depositional environment and negative Ce anomaly can also be present in certain types of diagenetic nodules (e.g. Nath et al. 1994 and references therein), but hydrogenous FeMn oxides would have well-defined and high positive Ce anomaly (Elderfield and Greaves 1981; Glasby et al. 1987; Nath et al. 1992) whereas diagenetic nodules have positive but show lesser Ce fractionation than hydrogenous nodules (Elderfield and Greaves 1981; Nath et al. 1994) and the hydrothermal FeMn precipitates would have negative Ce anomalies (Elderfield et al. 1981; Nath et al. 1997; Mascarenhas-Pereira and Nath 2010 and references therein). The Ce anomaly values of the three end-members (ESM Table 2) were used for mixing calculations (Eq. 2) to derive the contribution from these possible sources:

$$f_{\text{Hydrogenous}} + f_{\text{Hydrothermal}} + f_{\text{Diagenetic}} = 1 \quad (2)$$

and

$$\text{Ce anomaly}_{\text{mix}} = (f_{\text{Hydrogenous}} \times \text{Ce anomaly}_{\text{Hydrogenous}}) + (f_{\text{Hydrothermal}} \times \text{Ce anomaly}_{\text{Hydrothermal}}) + (f_{\text{Diagenetic}} \times \text{Ce anomaly}_{\text{Diagenetic}})$$

The mixing calculations have yielded relative contributions of the three end-members (see ESM Table 3 in the online electronic supplementary material). With increasing Ce anomaly the hydrogenous characteristics increase, while lower Ce anomaly corresponds with higher hydrothermal content. The Ce anomaly data were plotted with respect to the values used for the three end-members (Fig. 9; Ce/Ce\* values of 2.88, 0.27 and 1.27 for hydrogenous, hydrothermal and diagenetic signatures respectively). Thereby, three groups of samples were identified: (1) those with Ce/Ce\* of 0.7 to 0.8 fall near the

hydrothermal end-member field ( $n=5$ ), (2) a majority of samples with significant positive Ce anomalies ( $>1.9$ ) represent the hydrogenous end-member ( $n=4$ ) and (3) Ce anomalies (1.02 to 1.31) samples possibly representing either diagenetic or a mixture of hydrogenous-hydrothermal sources ( $n=11$ ).

Calculations using both the methods yielded high hydrothermal content (24 to 72%) for the FeMn oxides in all the samples indicating a plausible intrabasinal source. However, the above calculations should be considered as indicative and may not represent the actual proportions in which the elements were incorporated during the accretion of the oxides (cf. Chavagnac et al. 2005; Mascarenhas-Pereira and Nath 2010). The higher hydrothermal values for diagenetic samples in the mixing calculation are probably due to the plume fallout origin of the FeMn oxides. Since it is a three end-member calculation using Ce anomaly, diagenetic and plume fallout cannot be distinguished.

### 5.3 Source of hydrothermal activity

The nearest area of hydrothermal source could be from the adjoining seamounts either during their formation or from later eruptions (cf. Das et al. 2007) or due to incipient hydrothermal flows activity along the fracture zones (Iyer 1991). The fluids from these sources may have been channelled out as plume fallouts as also suggested by Mills et al. (2001) for the Trans-Atlantic Geotraverse samples.

The reported occurrence of ochrous sediments (with nontronite), volcanic magnetite spherules and volcanogenic-hydrothermal material (Iyer 2005 and references therein), geochemical proxies (Mascarenhas-Pereira and Nath 2010), aluminium-rich spherules and particles (Iyer et al. 2007), as well as autotrophic bacteria (Das et al. 2011) suggest prevalence of ubiquitous, albeit low-temperature hydrothermal activities in the CIOB. By using isotopic ( $^{210}\text{Pb}$ ,  $^{238}\text{U}$ - $^{230}\text{Th}$ ,  $^{10}\text{Be}$ ), major, trace elements, micromorphological and microchemical data; Nath et al. (2008) identified recent (100 years) hydrothermal alteration of a  $>200$  kyr sedimentary record from the flank of a seamount in the CIOB. Two other hydrothermal events corresponding to 10 ka (Iyer et al. 1997) and 625 ka (Iyer et al. 1999) had also occurred in the CIOB.

The pumices studied cover a broad area in the CIOB where hydrothermal activity seems to have been active. Sample 4 is close to seamount chain D along the  $79^\circ\text{E}$  fracture zone, and most of the plume fallout samples lie close to this location. Northwards along the same fracture zone lies sample 20, while samples 6 and 18 are along either side of the  $79^\circ\text{E}$  fracture zone and sample 17 is on the plain and close

to the 79°E fracture zone (Fig. 1). Therefore, it is clear that seamounts and/or fracture zones are congenial sites of hydrothermal events (Iyer 2005).

#### 5.4 Growth rate of FeMn oxides

Trace element concentrations in the FeMn oxides fluctuate due to the differences in their rate of precipitation and related scavenging processes (Kuhn et al. 2003). Hence, contents of Mn, Fe and trace elements could be useful markers for the growth rates of FeMn oxides (Halbach et al. 1983).

The empirical formulae of Lyle (1982) and Sharma and Somayajulu (1987) used for approximate age calculations are best suited for slow growth rates of FeMn oxides, whereas the Manheim and Lane-Bostwick (1988) formula is apt for fast growth rates. The calculated growth rates are 3 to 47 mm/10<sup>6</sup> years (avg. 10 mm/10<sup>6</sup> years) by Lyle (1982) which is higher than the one obtained using Sharma and Somayajulu (1987) method 3 to 27 mm/10<sup>6</sup> years (avg. 7 mm/10<sup>6</sup> years); whereas using Manheim and Lane-Bostwick (1988) gave the lowest growth rates 3 to 19 mm/10<sup>6</sup> years (avg. 5 mm/10<sup>6</sup> years). Samples #6, 17,18, 20, which have a hydrothermal affinity, show a faster growth rate (Table 2). The sample #18 with a maximum growth rate (47 mm/10<sup>6</sup> years) and a minimum age (0.07 Ma) indicates that accretion was enhanced manifold by an additional contributory source.

Higher growth rates for some of the nodules, crust and shark teeth have been noted in the CIOB (Banakar and Sudhakar 1988; Banakar and Borole 1989; Banerjee and Mukhopadhyay 1991; Prasad 1994; Iyer 1999) but no hydrothermal component was studied in those cases. It is believed that the accretion of these oxides is largely due to hydrogenetic-diagenetic processes. – Based on the present studies we identify hydrothermal input as another source for the FeMn oxides in some cases.

#### 5. 5 Source of pumice and age of FeMn oxides

Pumice reported from continental margin and mid-ocean environments are generally assigned an exotic origin but deep-sea pumice eruptions are not ruled out (Binns 2003). The pumice recovered from the CIOB were considered to be either drifted products of the 1883 Krakatau eruption (Iyer and Karisiddaiah 1988; Martin-Barajas and Lallier-Verges 1993; Mudholkar and Fujii 1995; Pattan et al. 2008) or derived from local intraplate volcanoes (Iyer and Sudhakar 1993; Mascarenhas-Pereira et al. 2006). The pumice that form the substrate for the FeMn oxides are much older and could belong to some earlier volcanic activity rather than the 1883 eruption of Krakatau (Mukherjee and Iyer 1999; Pattan et al. 2013). Vallier and Kidd (1977) after studying the volcanogenic sediments in the Indian Ocean

suggested that abundant silicic volcanic glass was derived during Miocene times. Based on  $^{230}\text{Th}_{\text{xs}}$  values and radiolarian stratigraphy, Sukumaran et al. (1999) favoured an in situ deposition of the CIOB glass shards consequent to sub-oceanic volcanic activities during periods of elevated glaciations. The morphology and silicic composition of the shards also attest to intra-plate volcanism as a source for these shards (Iyer 2005; Mascarenhas-Pereira et al. 2006).

It is reported that accretion of ferromanganese nodules in the CIOB was between Early Pliocene (3 Ma) and Late Miocene (8 Ma) (Mukhopadhyay et al. 2008). Whereas, the approximate age of commencement of formation of oxide layer over the CIOB pumice ranges between 0.04 and 8 Ma (Table 2). The oxides may not have started accreting immediately after the pumice settled on the seabed but the growth could have commenced after thousands of years. Obviously, in such a case the pumice substrate is older than the ages obtained by the empirical dates for the oxides.

The Toba tuff of Indonesia is divided into the youngest Toba tuff (YTT), the middle Toba tuff (MTT), the oldest Toba tuff (OTT) and the Haranggoal dacite tuff (HDT), and these have ages of ca. 0.074, 0.50, 0.84 and ca. 1.20 Ma respectively (Chesner 1998). Based on the bulk composition and mineral chemistry the substrate pumice in the CIOB perhaps formed between Late Miocene and Early Pleistocene from Java or Sumatra (Indonesian arc) (Pattan et al. 2013). The ages of the oxides in our samples, derived through empirical formulae (Table 2), correspond to Late Miocene to Late Pleistocene. While these ages obviously suggest that Krakatau cannot be the source for the coated pumice it is important to note that the accretion of the FeMn oxides over the pumice commenced from Late Miocene. Therefore, these pumices could be older than Late Miocene and perhaps are not from a single source and also the contributing volcanic episodes might have differed in space and time. During such a process pumices of different generations were produced which were later coated with FeMn oxides, through multi-accretionary processes.

## **6. Conclusions**

The investigations show that ~25% ( $n=169$ ) of the 676 studied CIOB pumice samples are coated with FeMn oxides. The oxides show a mixed hydrogenous-diagenetic nature and a few carry an imprint of hydrothermal-plume fallout components. Of the 20 samples selected for analyses, hydrothermal signatures are evident in five samples based on negative Ce anomalies and low Co/Zn ratios, whereas a plume fallout source is interpreted for six samples based on Mn/Fe vs. Co and Ce relationships and lower REE and trace element contents. Amongst the latter, two samples have a relatively lower Co and

Ce and also have vernadite, which can form as plume fallout particles. These six plume fallout samples also show peaks of goethite, magnetite, lepidocrocite and hematite in XRD. The signatures of hydrothermal activity in the CIOB have been recorded as signatures in the FeMn oxides on the pumices. The results obtained through mixing calculations also support this, but this method constrains the distinction between plume fallout and diagenetic end-members. Therefore, a multi-accretionary process of hydrogenous-hydrothermal/plume fallout- diagenetic is suggested for the formation of the FeMn oxides over the pumice. From the reconstructed ages it is inferred that coated pumice in the CIOB can in places be older than the 1883 Krakatau eruption.

### **Acknowledgements**

We thank the Directors for permission to publish this paper. We acknowledge the help received from V.K. Banakar and G. Parthiban (ICP-OES), V. Khedekar (SEM-EDS), G. Prabhu (XRD), B. Vijay Kumar (access to sample repository), S. Jai Sankar (sample locations), and T.G. Rao and M. Satyanarayanan (ICP-MS; National Geophysical Research Institute, Hyderabad). We are obliged to two anonymous reviewers for thoughtful comments and suggestions that helped to substantially improve the quality of the manuscript, and to the editors for their useful feedback. This work is a part of N.K.'s Ph.D. thesis, with financial assistance via the CSIR (New Delhi) Fellowship scheme. This is NIO's contribution # ???.

### **References**

- Albarède F (1995) Introduction to geochemical modeling. Cambridge University Press, New York, pp 1–50
- Balaram V, Rao TG (2003) Rapid determination of REEs and other trace elements in geological samples by microwave acid digestion and ICP-MS. *Atomic Spectros* 24:206–212
- Balashov YuA, Girin YuP (1969) On the reserve of mobile rare earth elements in sedimentary rocks. *Geochem Int* 7:649–659
- Banakar VK, Borole DV (1989) Growth rate and chemical composition of a manganese nodule from the EEZ of Seychelles. *J Geol Soc India* 33:253–258
- Banakar VK, Sudhakar M (1988) Ferro-manganese oxide growth on shark teeth from Central Indian Ocean Basin. *Indian J Mar Sci* 17:265–269
- Banerjee R, Mukhopadhyay R (1991) Nature and distribution of manganese nodules from three sediment domains of the Central Indian Basin, Indian Ocean. *Geo-Mar Lett* 11:39–43

- Binns RA (2003) Deep marine pumice from the Woodlark and Manus Basins, Papua New Guinea. In: White JDL, Smellie JL, Clague DA (eds) Explosive subaqueous volcanism. AGU, Washington, DC, Geophys Monogr Ser 140:329–343
- Bodeř S, Manceau A, Geoffroy N, Baronnet A, Buatier M (2007) Formation of todorokite from vernadite in Ni-rich hemipelagic sediments. *Geochim Cosmochim Acta* 71:5698–5716
- Burns R G, Burns V M, Stockman H (1983) A review of the todorokite-buserite problem: implications to the mineralogy of marine manganese nodules: *Amer Mineral* 68:972–980
- Burns RG, Burns VM (1979) Manganese oxides. In: Burns RG (ed) Marine minerals. Mineral Soc Am Short Course Notes 6:1–46
- Calvert SE, Price NB (1977) Geochemical variation in ferromanganese nodules and associated sediment from the Pacific Ocean. *Mar Chem* 5:43–74
- Canet C, Prol-Ledesma RM, Bandy WL, Schaaf P, Linares C, Camprubí A, Tauler E, Mortera-Gutiérrez C (2008) Mineralogical and geochemical constraints on the origin of ferromanganese crusts from the Rivera Plate (western margin of Mexico). *Mar Geol* 251:47–59
- Chavagnac V, German CR, Milton JA, Palmer MR (2005) Sources of REE in sediment cores from the Rainbow vent site (36°14'N, MAR). *Chem Geol* 216:329–352
- Chesner CA (1998) Petrogenesis of the Toba tuffs, Sumatra, Indonesia. *J Petrol* 39:397–438
- Crerar DA, Barnes HL (1974) Deposition of deep sea manganese nodules. *Geochim Cosmochim Acta* 38:279–300
- Cronan DS (1980) Manganese nodules and encrustations. In: Cronan DS, Underwater minerals. Academic Press, New York, pp 61–166
- Cronan DS, Moorby SA (1981) Manganese nodules and ferromanganese oxide deposits from the Indian Ocean. *J Geol Soc Lond* 138:527–539
- Das P, Iyer SD, Kodagali VN (2007) Morphological characteristics and emplacement mechanism of the seamounts in the Central Indian Ocean Basin. *Tectonophysics* 443:1–18
- Das A, Fernandes CEG, Naik S, Nath BN, Suresh I, Mascarenhas-Pereira MBL, Gupta SM, Khadge NH, Prakash Babu C, Borole DV, Sujith PP, Valsangkar AB, Mourya BS, Biche SU, Sharma R, LokaBharathi PA (2011) Bacterial response to contrasting sediment geochemistry in the Central Indian Basin. *Sedimentology* 58:756–784
- Dekov VM, Marchig V, Rajta I, Uzony I (2003) Fe-Mn micronodules born in the metalliferous sediments of two spreading centres: the East Pacific Rise and Mid-Atlantic Ridge. *Mar Geol* 199:101–121
- Elderfield H, Greaves MJ (1981) Negative cerium anomalies in the rare earth element patterns of the oceanic ferromanganese nodules. *Earth Planet Sci Lett* 55:163–170

- Elderfield H, Hawkesworth CJ, Greaves MJ, Calvert SE (1981) Rare earth element geochemistry of oceanic ferromanganese nodules and associated sediments. *Geochim Cosmochim Acta* 45:513–528
- Glasby GP, Stüben D, Jeschke G, Stoffers P, Garbe-Schönberg CD (1997) A model for the formation of hydrothermal manganese crusts from the Pitcairn Island hotspot. *Geochim Cosmochim Acta* 61:4583–4597
- Glasby GP (1972) The mineralogy of manganese nodules from a range of marine environments. *Mar Geol* 13:57–72
- Glasby GP, Gwozdz R, Kunzendorf H, Friedrich G, Thijssen T (1987) The distribution of rare earth and minor elements in manganese nodules and sediments from the equatorial and SW Pacific. *Lithos* 20:97–113
- Halbach P, Scherhag C, Hebisch U, Marchig V (1981) Geochemical and mineralogical control of different genetic types of deep-sea nodules from the Pacific Ocean. *Miner Deposita* 16:59–84
- Halbach P, Segl M, Puteanus D, Mangini A (1983) Co-fluxes and growth rates in ferromanganese deposits from central Pacific seamount areas. *Nature* 304:716–719
- Iyer SD (1991) Comparison of internal features and microchemistry of ferromanganese crusts from the Central Indian Basin. *Geo-Mar Lett* 11:44–50
- Iyer SD (1999) Ferromanganese oxides on sharks' teeth from Central Indian Ocean Basin. *Indian J Mar Sci* 28:263–269
- Iyer SD (2005) Evidences for incipient hydrothermal event (s) in the Central Indian Basin: a review. *Acta Geol Sinica* 79:77–86
- Iyer SD, Karisiddaiah SM (1988) Morphology and petrography of pumice from the Central Indian Ocean Basin. *Indian J Mar Sci* 17:333–334
- Iyer SD, Sudhakar M (1993) Co-existence of pumice and manganese nodule fields- evidence for submarine silicic volcanism in the Central Indian Basin. *Deep-Sea Res* 40:1123–1129
- Iyer SD, Prasad MS, Gupta SM, Charan SN (1997) Evidence for recent hydrothermal activity in the Central Indian Basin. *Deep-Sea Res* 44:1167–1184
- Iyer SD, Gupta SM, Charan SN, Mills OP (1999) Volcanogenic-hydrothermal iron-rich materials from the southern part of the Central Indian Ocean Basin. *Mar Geol* 158:15–25
- Iyer SD, Mascarenhas-Pereira MBL, Nath BN (2007) Native aluminium (spherules and particles) in the central Indian Basin sediments: implications on the occurrence of hydrothermal events. *Mar Geol* 240:177–184
- Kalangukar NG (2012) Petrology and petrochemisry of pumices from Central Indian Ocean Basin. PhD Thesis, Goa University, India

- Kalangutkar NG, Iyer SD, Ilangoan D (2011) Physical properties, morphology and petrological characteristics of pumices from the Central Indian Ocean Basin. *Acta Geol Sinica* 85:826–839
- Koschinsky A, Hein JR (2003) Uptake of elements from seawater by ferromanganese crusts: solid-phase associations and seawater speciation. *Mar Geol* 198:331–351
- Kuhn T, Bau M, Blum N, Halbach P (1998) Origin of negative Ce anomalies in mixed hydrothermal–hydrogenetic Fe–Mn crusts from the Central Indian Ridge. *Earth Planet Sci Lett* 163:207–220
- Kuhn T, Bostwick BC, Koschinsky A, Halbach P, Fendorf S (2003) Unusual enrichment of Mo in hydrothermal Mn precipitates: possible sources, formation and phase associations. *Chem Geol* 199:29–43
- Lyle M (1982) Estimating growth rates of ferromanganese nodules from chemical compositions: implications for nodule formation processes. *Geochim Cosmochim Acta* 46:2301–2306
- Manheim FT, Lane-Bostwick CM (1988) Cobalt in ferromanganese crusts as a monitor of hydrothermal discharge on the Pacific seafloor. *Nature* 335:59–62
- Martin-Barajas A, Lallier-Verges E (1993) Ash layers and pumice in the Central Indian Basin: relationship to the formation of manganese nodules. *Mar Geol* 115:307–329
- Mascarenhas-Pereira MBL, Nath BN, Borole DV, Gupta SM (2006) Nature, source and composition of volcanic ash in sediments from a fracture zone trace of Rodriguez Triple Junction in the Central Indian Basin. *Mar Geol* 229:79–90
- Mascarenhas-Pereira MBL, Nath BN (2010) Selective leaching studies of sediments from a seamount flank in the Central Indian Basin: resolving hydrothermal, volcanogenic and terrigenous sources using major, trace and rare-earth elements. *Mar Chem* 121:49–66
- Mills RA, Wells DM, Roberts S (2001) Genesis of ferromanganese crusts from the TAG hydrothermal field. *Chem Geol* 176:283–293
- Mudholkar A, Fujii T (1995) Fresh pumice from the Central Indian Basin: a Krakatau 1883 signature. *Mar Geol* 125:143–151
- Mukherjee AD, Iyer SD (1999) Synthesis of the morphotectonics and volcanic of the Central Indian Ocean Basin. *Curr Sci* 76:296–304
- Mukhopadhyay R, Ghosh AK, Iyer SD (2008) The Indian Ocean nodule field: geology and resource potential. In: Hale M (series editor) *Handbook of Exploration and Environmental Geochemistry*, vol 10. Elsevier, Amsterdam, pp 155–224
- Nath BN (1993) Rare earth element geochemistry of the sediments, ferromanganese nodule and crusts from the Indian Ocean. PhD Thesis, Goa University, India



Nath BN (2007) Processes of formation of ferromanganese nodules and crusts. In: Refresher course on marine geology and geophysics (22nd October to 2nd November 2007). National Institute of Oceanography, Dona Paula, Goa, Lecture notes, pp 63–69

Nath BN, Balaram V, Sudhakar M, Plüger WL (1992) Rare earth element geochemistry of the ferromanganese deposits from the Indian Ocean. *Mar Chem* 38:185–208

Nath BN, Roelandts I, Sudhakar M, Plüger WL, Balaram V (1994) Cerium anomaly variation in ferromanganese nodules and crusts from the Indian Ocean. *Mar Geol* 120:385–400

Nath BN, Plüger WL, Roelandts I (1997) Geochemical constraints on the hydrothermal origin of ferromanganese encrustations from the Rodriguez Triple Junction, Indian Ocean. In: Nicholson K, Hein JR, Bühn B, Dasgupta S (eds) *Manganese mineralization: geochemistry and mineralogy of terrestrial and marine deposits*. *Geol Soc Spec Publ* 119:192–221

Nath BN, Borole DV, Aldahan A, Patil SK, Mascarenhas-Pereira MBL, Possnert G, Ericsson T, Ramaswamy V, Gupta SM (2008)  $^{210}\text{Pb}$ ,  $^{230}\text{Th}$ , and  $^{10}\text{Be}$  in Central Indian Basin seamount sediments: Signatures of degassing and hydrothermal alteration of recent origin. *Geophy Res Lett* 35: L09603, doi:10.1029/2008GL033849

Nayak B, Das SK, Munda P (2013) Biogenic signature and ultra microfossils in ferromanganese nodules of the Central Indian Ocean Basin. *J Asian Earth Sci* 73:296–305

Pattan JN, Mudholkar AV, Jai Sankar S, Ilangovan D (2008) Drift pumice in the Central Indian Ocean Basin: geochemical evidence. *Deep-Sea Res I* 55:369–378

Pattan JN, Pearce, NJG, Parthiban G, Smith VC, Mudholkar AV, Rao NR (2013) The origin of ferromanganese oxide coated pumice from the Central Indian Ocean Basin. *Quat Int* 313–314:230–239

Prasad MS (1994) Australasian microtektites in a substrate: a new constraint on ferromanganese crust accumulation rates. *Mar Geol* 116:259–266

Sarkar C, Iyer SD, Hazra S (2008) Inter-relationship between nuclei and gross characteristics of manganese nodules, Central Indian Ocean Basin. *Mar Georesources Geotechnol* 26:259–289

Sharma P, Somayajulu BLK (1987) Composition, mineralogy and depositional history of nodules from world oceans. In: Rao TSS, Natarajan R, Desai BN, Narayanaswamy G, Bhat SR (eds) *Contributions in Marine Sciences, Dr. S.Z. Qasim, Sastyabdapurti felicitation volume*. National Institute of Oceanography, Goa, India, pp 355–390

Sharma R, Sankar SJ, Samanta S, Sardar AA, Gracious D (2010) Image analysis of seafloor photographs for estimation of deep-sea minerals. *Geo-Mar Lett* 30:617–626

Sudhakar M, Iyer SD, Mislankar PG (1992) Does pumice control on the characteristics and distribution of ferromanganese nodules in the Central Indian Basin? In: *Abstract Volume 29th International Geology Congress, 24 August–3 September 1992, Kyoto, Japan*, p 606

Sukumaran NP, Banerjee R, Borole DV, Gupta SM (1999) Some aspects of volcanic ash layers in the Central Indian Basin. *Geo-Mar Lett* 18:203–208

Takahashi Y, Manceau A, Geoffroy N (2007) Chemical and structural control of the partitioning of Co, Ce, and Pb in marine ferromanganese oxides. *Geochim Cosmochim Acta* 71:984–1008

Toth JR (1980) Deposition of submarine crusts rich in manganese and iron. *Geol Soc Am Bull* 91:44–54

Usui A, Bau M, Yamazaki T (1997) Manganese microchimneys buried in the Central Pacific pelagic sediments: evidence of intraplate water circulation? *Mar Geol* 141:269–285

Vallier TL, Kidd RB (1977) Volcanogenic sediments in the Indian Ocean. In Heirtzler JR, Bolli HM, Davies TA, Saunders JB, Sclater JG (eds) *Indian Ocean geology and biostratigraphy studies following DSD legs 22-29*. American Geophysical Union, Washington, pp 87–118

Vineesh TC, Nath BN, Banerjee R, Jaisankar S, Lekshmi V (2009) Manganese nodule morphology as indicators for oceanic processes in the Central Indian Basin. *Int Geol Rev* 51:27–44

Wang, X., Schröder, H.C., Schloßmacher, U., Müller, W.E.G., 2009b. Organized bacterial assemblies in manganese nodules: evidence for role of S-layers in metal deposition. *Geo-Mar Lett* 29:85–91

## Caption to figures

**Fig. 1** Location map showing occurrence of FeMn oxide-coated pumice in the Central Indian Ocean Basin. *FZ* Fracture zone, *A to H* seamount chains along propagative fracture zones, *IOTJ* Indian Ocean Triple Junction. Contour interval = 100 m (base map after Das et al. 2007)

**Fig. 2** Pumice showing variable thickness of FeMn oxides. **a** One side coated with up to 5-mm-thick botryoidal FeMn oxides. **b–d** Vesicles filled with FeMn oxide and with partly to fully coated surfaces

**Fig. 3** Electron micrographs of FeMn oxides on pumice. **a–c** Botryoids of different sizes. **d** Phillipsite crystal embedded in FeMn oxides

**Fig. 4** XRD plots of FeMn oxides for samples 1–20. Todorokite (T) is present in most of the samples whereas vernadite (V) is observed in a few, along with lepidocrocite (Lp), goethite (G), birnessite (Br), hematite (H) and magnetite (Mt). Quartz (Q) and plagioclase (P) occur as minor minerals. *Cps* Counts per second (hkl, Miller indices, given in brackets). Note that sample 12 could not be included in the heating experiment due to insufficient sample quantity

**Fig. 5** Ternary diagram of  $(\text{Co}+\text{Ni}+\text{Cu})\times 10\text{--Fe--Mn}$  (after Halbach et al. 1981), showing the CIOB coated pumice to fall in the hydrogenous and diagenetic fields

**Fig. 6** PAAS normalized REE patterns for FeMn oxides showing negative Ce anomaly for samples #4, 6, 17, 18, 20, whereas the remaining samples show positive Ce anomaly. For station numbers, see Table 1

**Fig. 7** A continuum between diagenetic, hydrothermal (with plume fallout, *PF*) and hydrogenous signatures”. Plots of **a** Mn/Fe vs. Co and **b** Mn/Fe vs. Ce

**Fig. 8** REE patterns using mass balance equations with variable proportions of hydrogenous, hydrothermal and diagenetic components (for more information, see main text)

**Fig. 9** Hypothetical cerium anomaly ( $\text{Ce}/\text{Ce}^*$ , ●, y axis) vs. proportions of hydrogenous:hydrothermal:diagenetic end-members (x axis) based on ternary mixing calculations: hydrogenetic FeMn crust (★), CIOB; hydrothermal Mn oxide (■), Lau Basin; diagenetic nodule (◆), CIOB.  $\text{Ce}/\text{Ce}^*$  0.7 to 0.9: dominant hydrothermal component;  $\text{Ce}/\text{Ce}^*$  >1.9: major hydrogenous source;  $\text{Ce}/\text{Ce}^*$  >1: either diagenetic or mixed hydrogenous–hydrothermal sources (see main text)

## Captions to Tables

**Table 1** Locations of samples 1–20 and nature of pumice coated with FeMn oxides, Central Indian Ocean Basin. *SC* Seamount chain, *smt* seamount, *FZ* fracture zone, *hydro* hydrogenetic, *hydroth* hydrothermal, *plume* plume fallout, *diag* diagenetic, *na* not available. For convenience, the serial numbers are used in the subsequent tables and text

**Table 2** Contents of Fe and Mn, growth rates calculated by the empirical formulae of (1) Lyle (1982), (2) Sharma and Somayajulu (1987) and (3) Manheim and Lane-Bostwick (1988), and corresponding age of commencement of oxide formation for samples 1–20

**Table 3** REEs (ppm) of FeMn oxides on CIOB pumice, compared with values for the USGS NOD A-1 reference standard

Table 1: Locations of samples 1–20 and nature of pumice coated with FeMn oxides, Central Indian Ocean Basin. *SC* Seamount chain, *smt* seamount, *FZ* fracture zone, *hydro* hydrogenetic, *hydroth* hydrothermal, *plume* plume fallout, *diag* diagenetic, *na* not available. For convenience, the serial numbers are used in the subsequent tables and text

Sample No	Station	Latitude (°S)	Longitude (°E)	Water depth (m)	Fe-Mn oxide coating	Location	Origin
Sample 1	AAS 26# 44	12.96	75.50	5280	1 mm oxides	S.C.,	plume
Sample 2	AAS 26# 13	12.54	75.62	5375	1 mm oxides	Betwn S.C.	diag
Sample 3	AAS 26# 36	12.97	75.47	5270	partly coated 1 mm oxides	S.C.	diag
Sample 4	AAS 26# 14	12.52	75.52	5230	1 side coated 1 mm oxides	F.Z.	Hydroth-plume
Sample 5	AAS 26# 43	12.98	75.51	5265	1 side coated thick botryoidal oxide upto 2 cm	S.C.	hydrog
Sample 6	SS3/135	10.51	79.50	5340	Patchy 2 mm botryoids	Plain	hydroth
Sample 7	AAS 3/B15/57	10.54	75.21	5281	1 mm patch on flat side	Smt,	diag
Sample 8	SK23/255B	9.99	78.97	5260	Coated 1 mm	F.Z.,	diag
Sample 9	AAS 26# 19	12.74	75.75	5350	3 mm thick oxide on 1 side botryoidal (5 mm)	S.C.	hydrog
Sample 10	AAS 3/B15/69	12.73	75.70	5305	oxide in vesicles and 1 mm thick cover	S.C.	hydrog
Sample 11	AAS 26# 27	12.71	75.72	5360	2 mm oxides on one side	S.C.	plume
Sample 12	AAS 26#12	12.67	75.67	na	2 mm oxides	F.Z.	plume
Sample 13	SS13/ 704B	12.50	79.25	5300	Patchy	Plain	plume
Sample 14	AAS3/B15/ 60	10.60	75.13	5250	3 mm coated on 1 side	Smt	plume
Sample 15	SS13/ 683	13.51	76.00	5250	fully coated 4 mm on 1 side	Betwn S.C.	diag
Sample 16	AAS3/ B15/ 59	12.71	75.70	5321	2 mm mammilated, 1 mm on other side	S.C.	plume
Sample 17	SK 23/ 256 AEG	10.02	77.98	5240	Patchy 2-5 mm oxides	Plain	hydroth
Sample 18	SK 23/255 CD	9.99	78.97	5238	fully coated 2 mm oxides	F.Z.	hydroth
Sample 19	AAS 26# 43	12.98	75.51	5265	1 side coated thick botryoidal 1 mm	S.C.	hydrog
Sample 20	F1/7D	11.01	75.49	na	2 mm thick patches of oxides	Plain	hydroth

Table 2: Contents of Fe and Mn, growth rates calculated by the empirical formulae of (1) Lyle (1982), (2) Sharma and Somayajulu (1987) and (3) Manheim and Lane-Bostwick (1988), and corresponding age of commencement of oxide formation for samples 1–20

No.	Thickness (mm)	Mn (%)	Fe (%)	Mn/Fe	Co/Zn	Growth rate (mm/10 <sup>6</sup> years)			Age (Ma)		
						(1)	(2)	(3)	(1)	(2)	(3)
1	1	10.02	4.55	2.20	1.95	8	6	4	0.16	0.12	0.25
2	1	21.15	6.39	3.31	1.93	9	6	4	0.15	0.11	0.23
3	1	17.32	4.92	3.52	1.94	12	8	4	0.12	0.08	0.27
4	1	3.47	3.34	1.04	0.73	5	5	11	0.21	0.18	0.08
5	20	20.24	11.04	1.83	4.34	3	3	3	5.64	6.44	7.9
6	2	22.96	4.57	5.02	1.10	18	11	6	0.18	0.11	0.35
7	1	17.4	9.35	1.86	2.57	4	4	5	0.26	0.28	0.21
8	1	17.38	7.42	2.34	2.22	5	5	4	0.2	0.18	0.23
9	3–5	21.68	11.62	1.87	3.93	3	3	3	0.86–1.43	0.99–1.66	1.03
10	1	14.52	9.81	1.48	2.67	3	3	4	0.29	0.35	0.24
11	2	9.12	5.07	1.80	1.99	6	5	4	0.39	0.33	0.47
12	2	14.88	5.31	2.80	1.68	9	7	5	0.31	0.22	0.37
13	2	10.07	3.97	2.54	1.24	11	7	5	0.27	0.19	0.38
14	3	9.02	5.1	1.77	1.18	6	5	9	0.59	0.50	0.34
15	4	16.21	6.2	2.61	2.19	7	6	4	0.71	0.56	0.98
16	2	5.63	4.01	1.40	1.56	6	5	5	0.39	0.33	0.38
17	2–5	24.79	4.19	5.92	0.91	23	14	8	0.14–0.36	0.09–0.22	0.24
18	2	29.79	3.18	9.37	0.51	47	27	19	0.07	0.04	0.10
19	1	19.53	11.22	1.74	4.41	3	3	3	0.29	0.34	0.37
20	2	24.91	4.22	5.90	0.66	23	14	10	0.14	0.09	0.20
Avg.		16.50	6.30	3.00	1.98						

Table 3. REEs (ppm) of FeMn oxides on CIOB pumice, compared with values for the USGS NOD A-1 reference standard

	<b>La</b>	<b>Ce</b>	<b>Pr</b>	<b>Nd</b>	<b>Sm</b>	<b>Eu</b>	<b>Gd</b>	<b>Tb</b>	<b>Dy</b>	<b>Ho</b>	<b>Er</b>	<b>Tm</b>	<b>Yb</b>	<b>Lu</b>
	NOD A-1													
	118.00	732.00	21.70	94.00	21.10	4.96	26.10	4.20	22.80	5.80	11.70	2.19	13.80	2.24
Avg.	118	733	22	94	21	5	26	4	23	6	12	2	14	2
Error%	0	0	0	0	-1	-1	2	0	1	0	0	0	-1	-1
	CIOB samples 1-20													
1	62	175	16	69	17	4	16	3	14	3	6	1	7	1
2	97	257	27	114	30	7	27	5	23	5	9	2	10	2
3	87	215	21	89	22	5	20	3	16	3	6	1	8	1
4	35	53	8	33	8	2	7	1	7	2	4	1	5	1
5	205	841	51	215	54	12	51	9	44	9	17	3	20	3
6	68	154	20	85	22	5	19	3	16	3	6	1	8	1
7	123	343	33	137	35	8	33	6	28	6	11	2	14	2
8	101	295	28	117	30	7	27	5	23	5	9	2	11	2
9	192	903	49	206	51	12	49	8	40	9	16	3	18	3
10	138	624	36	153	39	9	37	6	31	6	12	2	14	2
11	73	214	19	80	20	5	18	3	16	3	7	1	8	1
12	68	162	18	75	20	5	17	3	14	3	6	1	7	1
13	40	100	11	46	12	3	10	2	9	2	4	1	5	1
14	58	143	15	61	16	4	14	3	13	3	5	1	6	1
15	75	216	20	86	22	5	21	4	18	4	7	1	9	1
16	44	95	10	42	10	3	9	2	8	2	3	1	4	1
17	64	130	19	79	21	5	18	3	16	3	7	1	8	1
18	61	114	18	77	20	5	17	3	15	3	6	1	7	1
19	194	818	49	204	52	12	49	8	42	9	17	3	20	3
20	71	128	20	88	24	5	20	4	18	4	7	1	8	1
Avg.	95	372	23	97	24	6	23	4	20	5	9	2	10	2

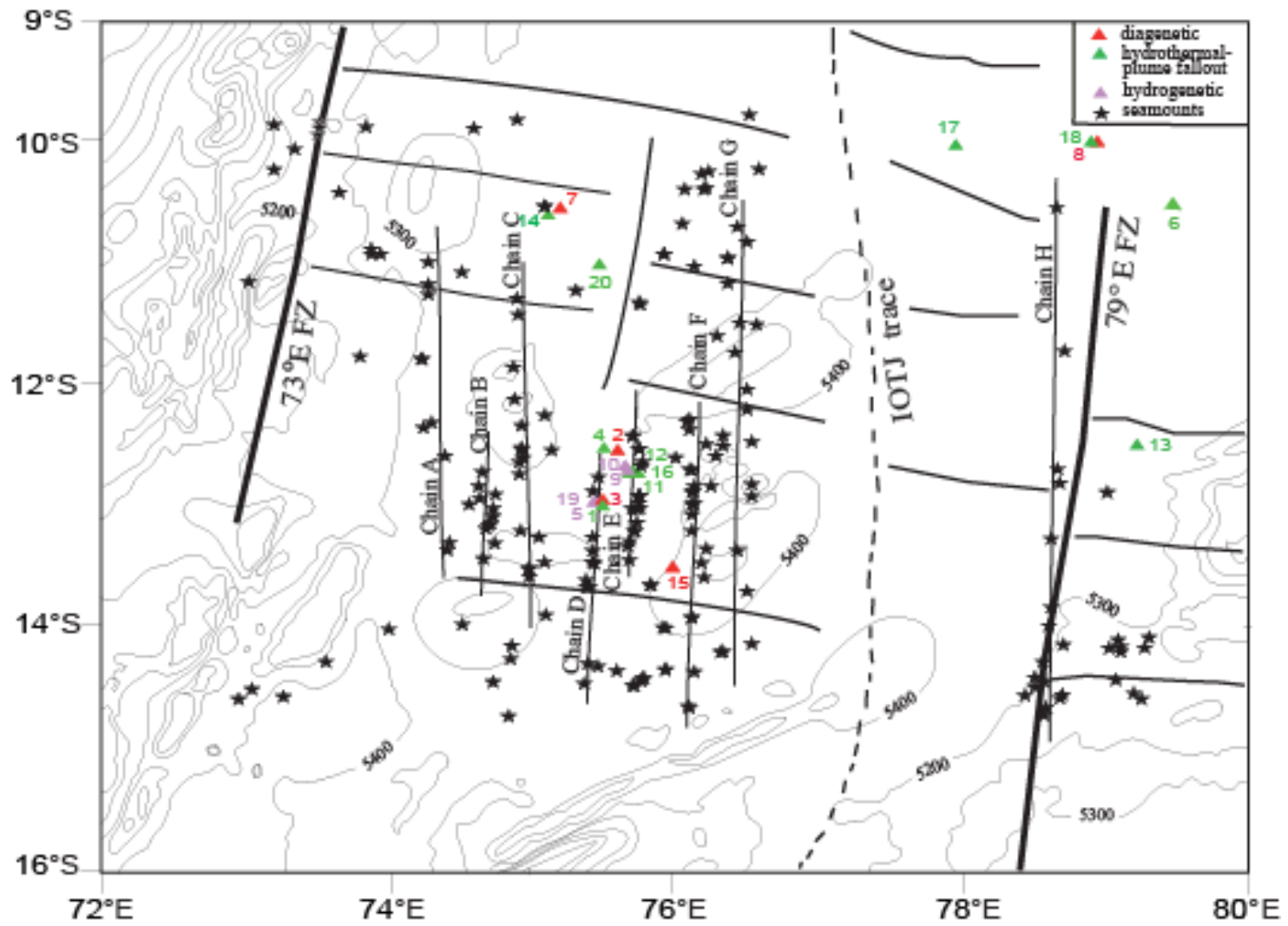


Fig. 1





AAS26/43



SK 23/263 G



F1/7D



F1/7E, 7B

Fig. 2

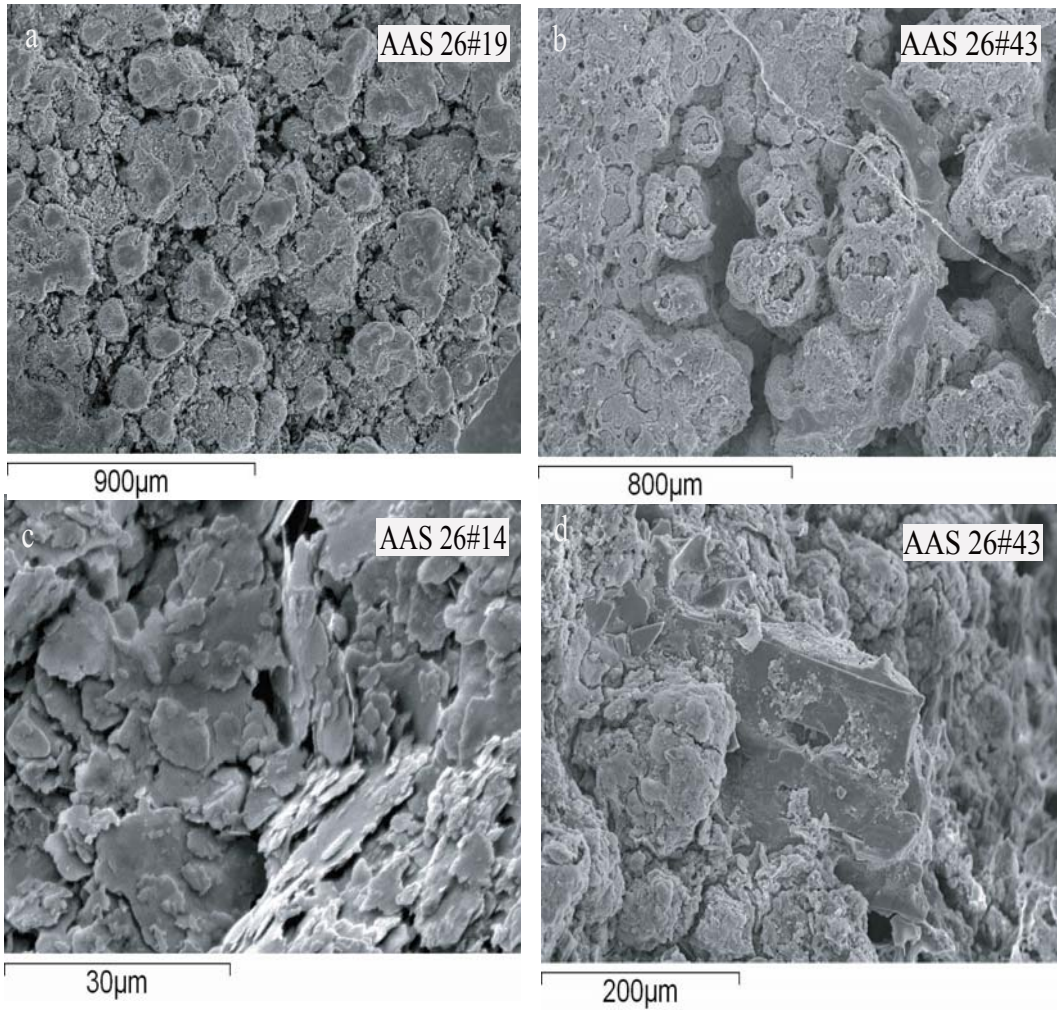


Fig. 3

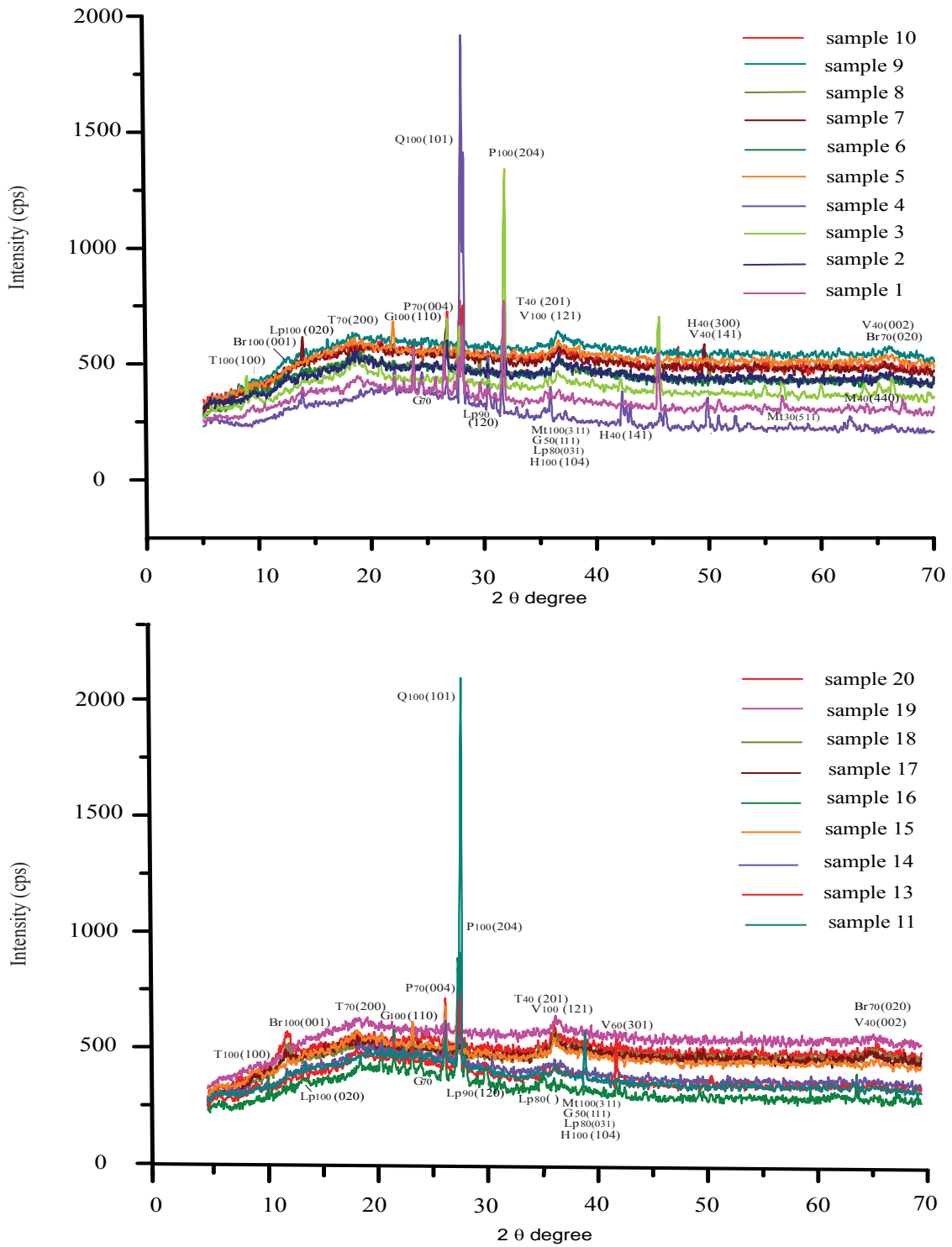


Fig. 4

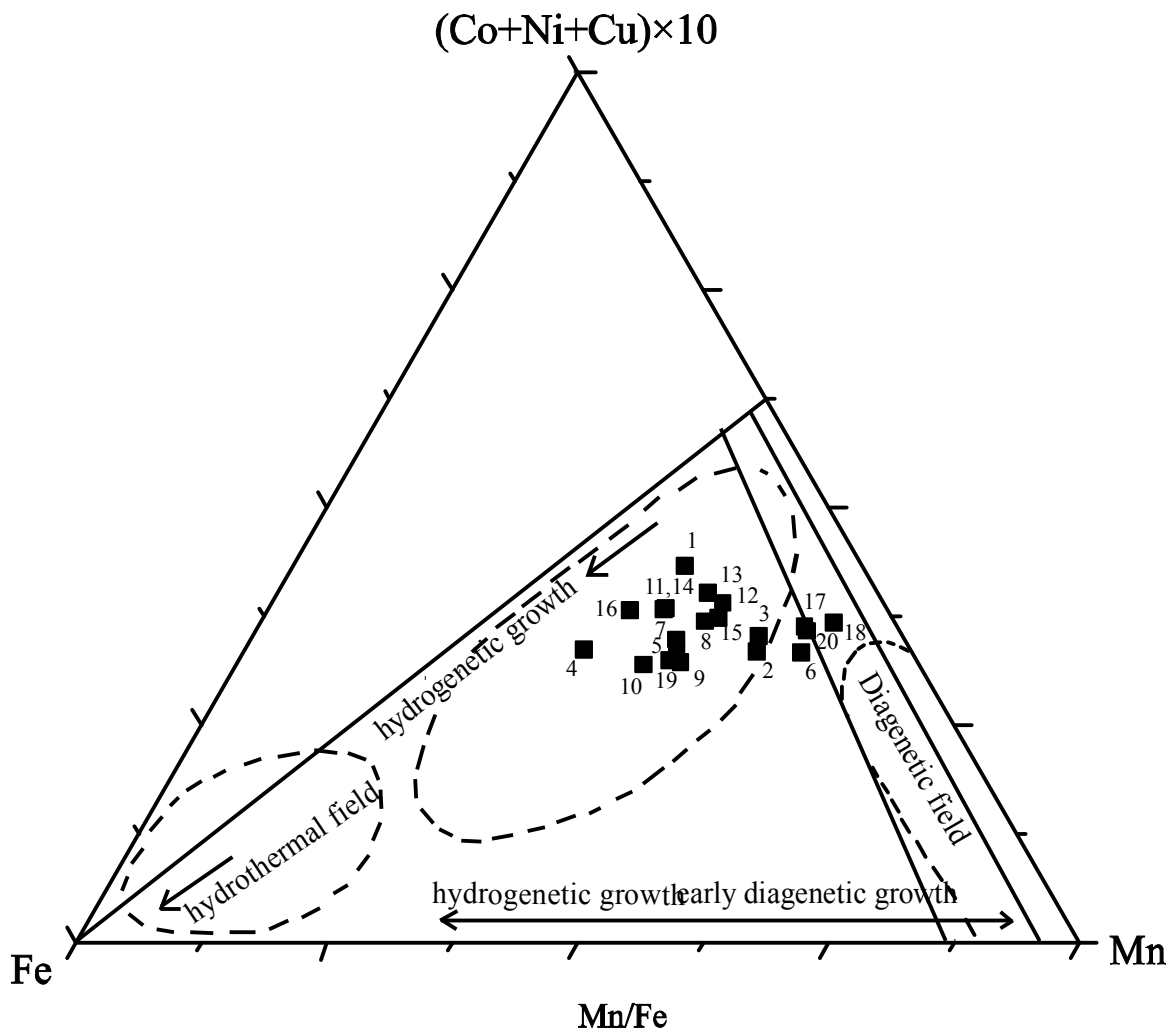


Fig. 5

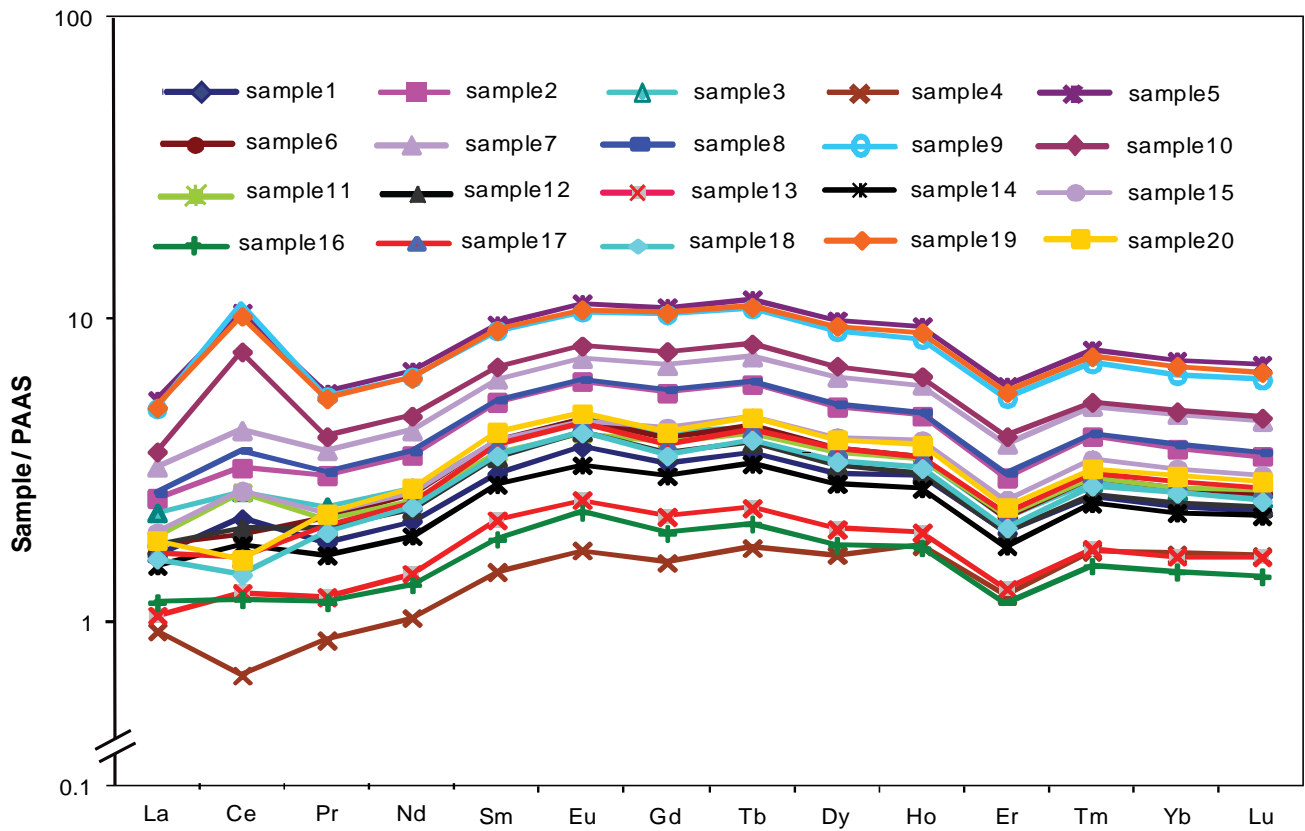


Fig. 6

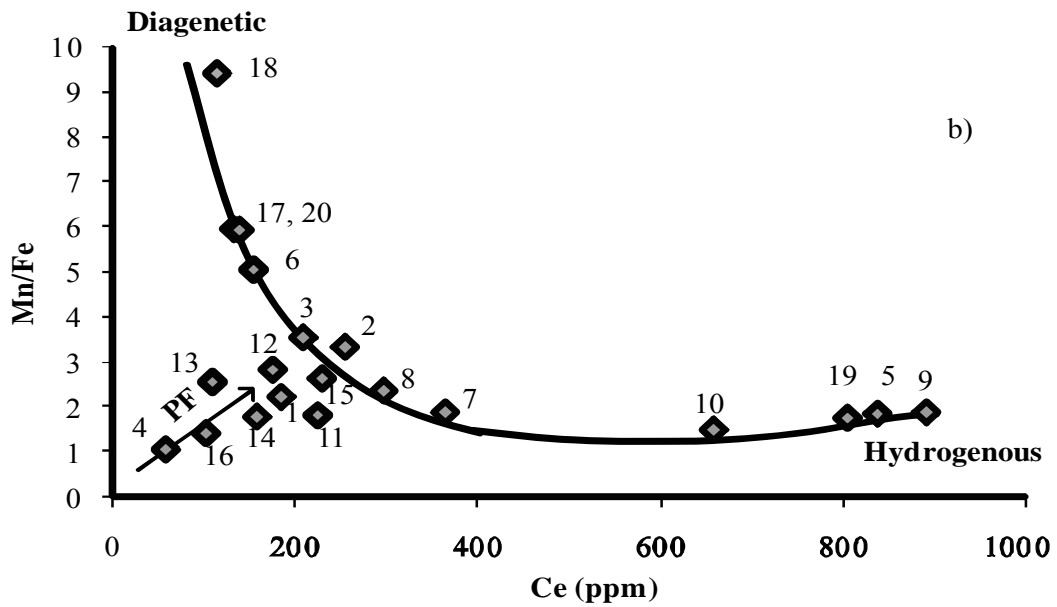
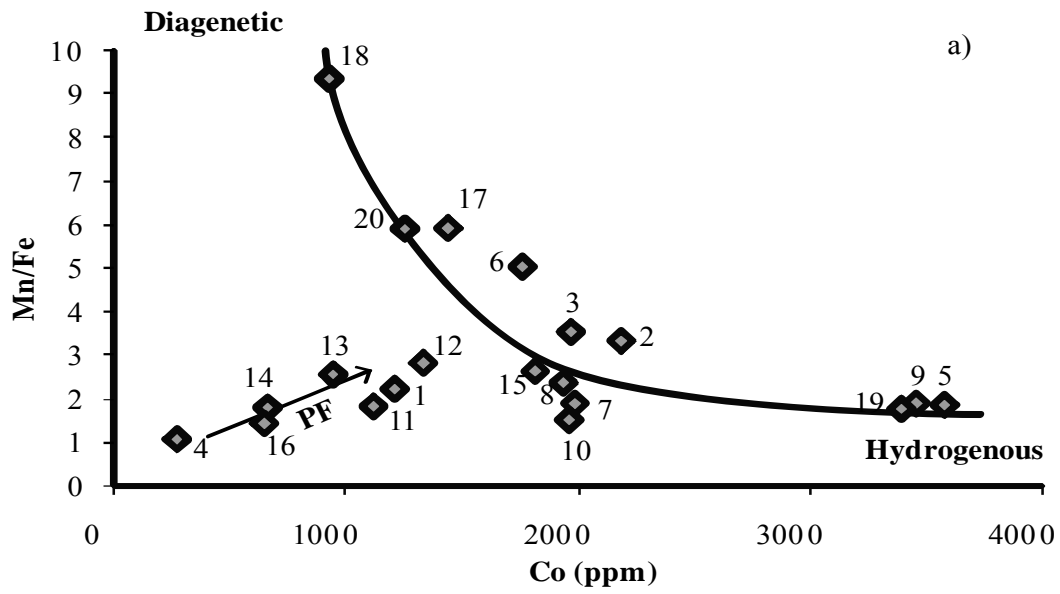


Fig. 7

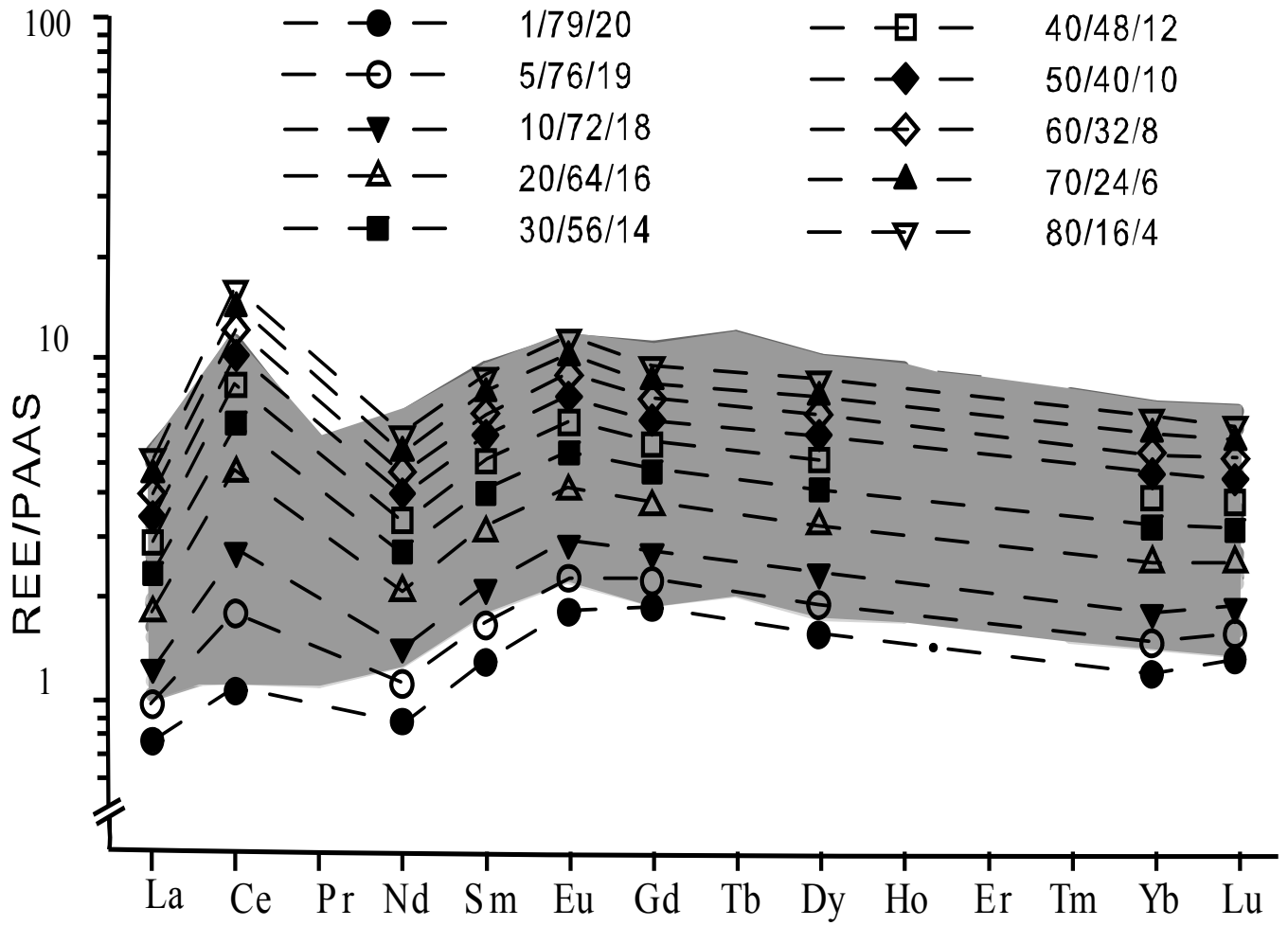


Fig. 8

